NJC

ROYAL SOCIETY OF CHEMISTRY

PAPER

View Article Online
View Journal | View Issue

Cite this: *New J. Chem.*, 2021, **45**, 13056

A tunable temperature-responsive and tough platform for controlled drug delivery†

Shuting Gao,[a] Aying Zhou,[a] Bin Cao,[a] Jing Wang,[b] Fanghua Li,[a] Guosheng Tang,[a] Zhicheng Jiang,[a] Anquan Yang,[b] Ranhua Xiong,*[c] Jiandu Lei *[d] and Chaobo Huang *[ae]

Localized intelligent drug delivery systems (IDDSs) are promising platforms for solid tumor therapy with lower toxicity to physiological systems and improved curative effects due to efficiently controlled site-specific delivery of therapeutic molecules. To this end, a temperature-responsive tailorable fibrous localized drug-delivery system with enhanced mechanical properties to withstand the stress *in vivo* and temporal loading regimes for cancer treatment is developed. A series of PCM-functionalized PU–PCL core–shell fiber mats are prepared by coaxial electrospinning, which exhibit a tunable temperature response and controlled release capability. The *in vitro* release profiles observably show faster release of encapsulated molecules above 39 °C than that at lower temperatures under the same conditions and the study proves that the release conforms to biphasic release kinetics. The release profiles could be subtly regulated *via* tuning the mass fraction of the PCM. More importantly, the result of cytotoxicity assay shows the viability of cancer cells after treatment with hydroxycamptothecin (HCPT) release media at different temperatures and indicates that media containing HCPT released at 39 °C could kill significantly more cancer cells than those released below 39 °C, which confirms the temperature sensitivity of the prepared IDDSs. This work thus provides a promising intelligent platform for site-specific drug-delivery in solid tumor therapy.

Received 20th March 2021,
Accepted 14th May 2021

DOI: 10.1039/d1nj01356d

rsc.li/njc

1. Introduction

Traditional drug delivery systems have encountered great challenges and exposed defects such as dissatisfactory release time, ineffective and inaccurate delivery to the site of lesions, toxic side effects, *etc.* Accordingly, a vast effort has been dedicated to intelligent drug delivery systems (IDDSs), which are designed to adjust the site and/or the release rate to the *in vivo* physiological conditions of the patient, to the progression of the illness, or to the circadian rhythms.[1] IDDSs are able to change conformations and other physicochemical properties in response to external stimuli (temperature, light with various wavelengths, mechanical signals, magnetic or electric fields, *etc.*) or *in vivo* physiological conditions (pH, ionic strength, biomolecules, *etc.*).[2] Compared with traditional systems, IDDSs reveal distinctive superiorities: (i) relatively stable drug concentrations in plasma, (ii) significantly higher drug efficiency with lower dosage, and (iii) targeted delivery minimizing the toxic side effects of the drug. To this end, developing an intelligent drug-delivery system is significantly desirable.

Nano-scale materials have been widely investigated for IDDSs.[3] Among them, electrospun nanofibers have attracted extensive attention for their higher drug encapsulation efficiency, flexibility in surface functionalities, stability and simple procedure. The mild process conditions enable the electrospinning technique to easily maintain the structural integrity and bioactivity of the encapsulated drugs and the release profiles are able to be adjusted by choosing various polymer matrixes.[4] Importantly, electrospun materials provide feasibility of site-specific drug delivery in cancer treatment, which can decrease the inevitable side effects induced by chemotherapeutics.[5,6] For instance, Zhang *et al.* indicated that drug-loaded polylactide electrospun fibers show higher efficiency in diminishing solid tumors than free drugs treated systematically.[7,8] However, due to the rapid evaporation of solvent and the high ionic strength in solution, most drug compounds tend to accumulate on or near the fiber surface, leading to the significant explosive release of the electrospun nanofiber carrier at the initial stage.[9,10] To overcome this problem,

[a] *College of Chemical Engineering, Jiangsu Co-Innovation Center of Efficient Processing and Utilization of Forest Resources, Nanjing Forestry University, Nanjing, 210037, P. R. China. E-mail: huangchaobo@njfu.edu.cn*
[b] *OSM Biological Co., Ltd, Deqing, 313200, P. R. China*
[c] *Lab General Biochemistry & Physical Pharmacy, Department of Pharmaceutics, Ghent University, 9000, Belgium*
[d] *Beijing Key Laboratory of Lignocellulosic Chemistry, and MOE Engineering Research Center of Forestry Biomass Materials and Bioenergy, Beijing Forestry University, Beijing, 100083, P. R. China*
[e] *Joint Laboratory of Advanced Biomedical Technology (NFU-UGent), Laboratory of Biopolymer Based Functional Materials, Nanjing Forestry University, Nanjing, 210037, P. R. China*

† Electronic supplementary information (ESI) available. See DOI: 10.1039/d1nj01356d

coaxial electrospinning has been designed to provide single fiber core/shell structures that can alleviate burst release.[11,12] More importantly, electrospun fibers with core–shell structure showed sustained release of drugs.[13] They can release encapsulated drugs both rapidly and sustainably from a single platform in different timescales.[14,15]

On the basis of the aforementioned, we have designed a simple temperature-responsive localized drug-delivery platform with enhanced mechanical properties for cancer treatment *via* coaxial electrospinning. Poly(ε-caprolactone) (PCL) is non-cytotoxic and biodegradable, which is extensively studied for drug delivery due to its compatibility with a wide range of drugs. Hence, we used PCL as the sheath of the fibers for its prominent properties.[16] Polyurethane (PU) exhibits distinguished mechanical properties owing to its thermodynamic incompatibility between soft and hard segments in the main chains.[17] Herein, PU (core) is to improve the strength and tenacity of the fibers, which can enable the IDDS to easily withstand the stress *in vivo* and temporal loading regimes after being implanted. We introduced a phase-change material (PCM, eutectic mixture of lauric acid and stearic acid derived from natural fats) that can reversibly realize a solid–liquid phase transition according to temperature variation to allow the temperature-responsive release of drugs from the core–shell electrospun nanofibers. Among the various kinds of PCMs (such as tetradecanol, hexadecanol, L-menthol, *etc.*), natural fatty acids (lauric acid and stearic acid) are particularly attractive because of the low cost, high stability, biocompatibility and biodegradability.[18–21] On account of the impact of temperature on normal tissues, it is significant to use PCMs with a phase-change temperature close to the physiological temperature of the human body (37 °C).[2,22] Herein, we investigated a series of eutectic mixtures of lauric acid and stearic acid with different ratios to get a single melting point at 38–39 °C. Below the phase-change temperature, the PCM will keep in the solid state, leading to slow diffusion of the drug. When it is slightly higher than the phase-change temperature, the PCM will change to the liquid phase quickly and reversibly, accelerating the release rate of the encapsulated drugs (Scheme 1). Additionally, the release profiles can be subtly regulated *via* tuning the mass fraction of the PCM. From the above, we have successfully prepared a biocompatible temperature-controlled tailorable fibrous site-specific drug release platform for tumor chemotherapy and the study of the release profiles indicates that the IDDS allows for fast and slow biphasic release kinetics, which has potential in multi-drug packaging for synergistic therapies on solid tumors.

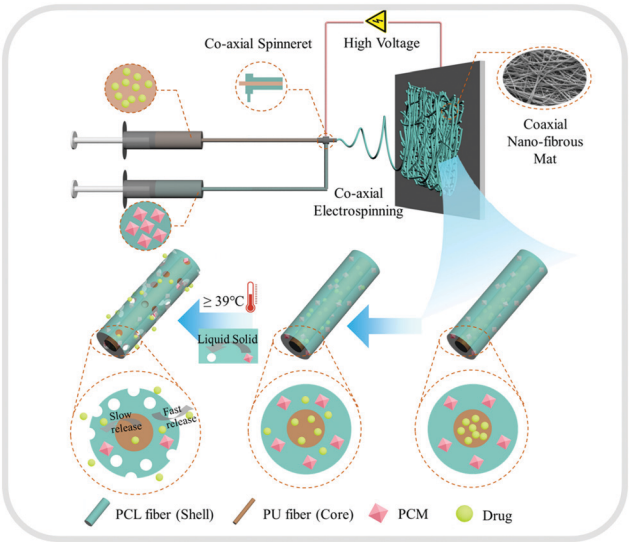

Scheme 1 Schematic representation of PCM-functionalized PU–PCL coaxial nanofiber mat fabrication and controllable release of drug molecules.

2. Materials and methods

2.1. Materials

Lauric acid (LA, 98%), stearic acid (SA, 99%), poly(ε-caprolactone) (PCL, M_w = 80 000 g mol^{-1}), polyurethane (PU, M_w = 100 000 g mol^{-1}), rhodamine B (99%), chloroform (AR, 99%), *N*,*N*-dimethylformamide (DMF) (AR, 99%), hydroxycamptothecin (HCPT, 98%) and MTT kits were purchased from Aladdin (Shanghai, China). The chemicals were used without further purfication. L929 cells and liver hepatocellular carcinoma (HepG2) cells were purchased from BioCambridge (Nanjing, China).

2.2. Preparation of eutectic mixtures of LA and SA

LA and SA at different mixing ratios were put into a beaker and heated under magnetic stirring (600 rpm). After heating at 90 °C for 0.5 h, the samples were cooled down to room temperature in air. After grinding at 25 °C, the samples were dried in a vacuum oven for 10 h.

2.3. Fabrication of PCM-functionalized core–shell electrospun nanofibers

PU (core)–PCL (sheath) fibers were obtained *via* coaxial electrospinning a PCL solution (22%, wt/v; *N*,*N*-dimethylformamide (DMF)/chloroform (1 : 9, v/v) as a solvent) and a PU solution (12%, wt/v; DMF as a solvent). Rhodamine B as a model drug and PCM (mixture of lauric acid and stearic acid prepared before) were added to the PU solution and PCL solution before electrospinning, respectively. The mass fractions of the mixture of LA and SA to PCL (f_{PCM}) were set at 0.05 and 0.1. The core and sheath solutions were fed in 1 mL syringes individually and connected *via* a coaxial needle (25 G (inner), 18 G (outer)). The feed rate of the core (PU) and sheath (PCL) solutions was set at 0.3 and 0.6 mL h^{-1}, respectively. A positive voltage was applied at 13–15 kV. The distance between the revolving flywheel to collect the fibers and the coaxial needle was kept at 12 cm. For the cell viability test, pure core–shell fibers and HCPT loaded core–shell fibers were also prepared under the same conditions. As a control, pure PCL and PU fibers were fabricated using the same parameters as coaxial electrospinning.

2.4. Cell culture

L929 cells and HepG2 cells were cultured in Dulbecco's modified Eagle's medium (DMEM) with 10% fetal bovine serum (FBS). The cultures were maintained in a humid atmosphere at 37 °C under

5% CO_2 and 95% air. The culture medium was replaced per two or three days.

2.5. Cell viability test

To test the cytotoxicity of the prepared electrospun core–shell fibers, we used L929 cells. The cells were seeded in 96-well cell culture plates (6000 cells per well) for 24 h. To make extracts from the fibers (1 mL DMEM was used to extract 0.5 cm^2 fibrous membrane), the fibers were immersed in DMEM at 37 °C for 72 h. After filtering (0.22 μm filters), the extracts were diluted using fresh DMEM. The cells were incubated with the (diluted) extracts at 37 °C. After 24 h, 20 μL MTT reagent (5 mg mL^{-1}) was added to each well, and then the cells was incubated at 37 °C for 4 h. Next, the medium was carefully removed and 150 μL DMSO was added into each well to dissolve the formazan crystals by incubating on a shaker for 20 min. Finally, the absorbance of each well was detected using a microplate reader at 492 nm (BIO-TEK, EL800). The viability (relative growth rate, RGR) of the L929 cells was obtained *via* comparing with that of untreated cells (which represents 100% viability). The RGR was defined as:

$$\mathrm{RGR} = A_e/A_p \times 100\% \quad (1)$$

A_e is the absorbance of the experimental groups, and A_p is the absorbance measured in the untreated group.

To evaluate the temperature-responsive release of HCPT loaded core–shell fibers, we used HepG2 cells. The cells were seeded in 96-well cell culture plates (6000 cells per well) for 24 h. The fibers were immersed in DMEM at 25, 37 and 39 °C for 24 h, respectively. The HepG2 cells were incubated with the sterilized release media for 24 h and 48 h, respectively. MTT assay was employed to quantify the cell viability using the same conditions used for L929 cells.

2.6. *In vitro* drug release studies

To evaluate the release of rhodamine B from the core–shell electrospun fibers, several fiber mats with the same weight were dipped in 10 mL PBS buffer solution (pH 7.4) at 25, 37 and 39 °C in a water-bath constant temperature vibrator (90 rpm). At specified time intervals, 3 mL release media was taken out for measurement (the concentration of rhodamine B was measured using a UV-vis spectrophotometer at λ = 553 nm) and 3 mL fresh PBS was then supplemented. The cumulative release of rhodamine B was calculated with eqn (2):

$$\mathrm{CR}\ (\%) = \frac{10C_n + 3\sum C_{n-1}}{m_0} \times 100 \quad (2)$$

where C_n and C_{n-1} represent the concentration of rhodamine B in the PBS buffer solution at n and $n-1$ times, respectively. n is the time of taking out the media and m_0 (mg) represents the content of rhodamine B encapsulated in the electrospun fibers.

2.7. Hemolysis activity assay

2 mL anticoagulant sheep whole blood and 4 mL PBS were added into a centrifuge tube, followed by centrifuging at 1000 rpm for 10 min. The surpernatant was taken out and 10 mL PBS was added into the centrifuge tube. The above operations were repeated 3 times. After centrifugation, the supernatant was taken out and the red blood cells were obtained. 7 mL PBS was added into the cell pellet to prepare the red blood cell suspension. 500 μL red blood cell suspension and 500 μL sample extract (5 mL PBS was used to extract 100 mg fibrous membrane) were added into centrifuge tubes, followed by shaking mildly in a thermostatic oscillator for 1 h at 36 °C. After centrifuging at 10 000 rpm for 2 min, 100 μL solution was transferred into a 96 well plate and the absorbance of the top clear layer was measured using an ultraviolet spectrophotometer at 540 nm. PBS was used as a negative control and 0.1% Triton X-100 was used as a positive control. The emolysis ratio (HR) was calculated using the following equation

$$\mathrm{HR} = \mathrm{AS/AP} \times 100\% \quad (3)$$

where AS is the absorption value of the samples and AP is the absorption value of the positive reference.

2.8. Characterization of the electrospun fibers

Dried electrospun fibers were imaged by field emission scanning electron microscopy (FE-SEM) (JSM-7600F, Hitachi, Japan). Transmission electron microscopy (TEM) images of the coaxial fibers were obtained *via* a TEM-2100 (Jeol, Japan) microscope. Differential scanning calorimetry (DSC) curves of the fiber membranes were measured in N_2 from 20 °C to 80 °C at 10 °C min^{-1} (V4.5A, America). The sample weight was 3–5 mg. The mechanical strength test of the fiber membranes was performed with a commercial test machine (Sans, UTM6502, Shenzhen, China). The samples (25 mm × 5 mm) were tested at a speed of 2 mm min^{-1}. The Young's modulus of the fiber membranes was manually calculated according to the linear region of the stress–strain curve at 5% strain. An inverted fluorescence microscope (IX53, OLYMPUS, Japan) was employed to observe the fluorescent fibers. Fourier transform infrared (FT-IR) spectra of the electrospun fibers were obtained using a VERTEX 80 v FT-IR spectrometer from 4000 to 500 cm^{-1}. X-Ray diffraction (XRD) patterns were obtained using an X-ray diffractometer (Ultima IV, Rigaku, Japan) over a Bragg angle from 10° to 50° (Cu-Kα) at a scan rate of 2° min^{-1}.

2.9. Statistical analysis

All data are expressed as mean ± standard error (n = 3). Statistical significance was analyzed by Student's t test with a 95% confidence level. Statistical significance was shown as $^{***}p < 0.001$; $^{**}p < 0.01$; $^{*}p < 0.05$.

3. Results and discussion

3.1. Preparation and characterization of the PCM

To evaluate the thermal property of the PCM, differential scanning calorimetry (DSC) thermograms were analyzed. Fig. S1a (ESI†) exhibits the DSC curves of the mixtures of LA and SA with different mass ratios (M) of LA to SA. Two or more peaks were observed in each thermogram and the melting point was

decreased with increasing mass ratio when the mass ratio exceeded 5 : 5, while a single peak appeared in each curve in the case of $M \leq 5:5$. Importantly, when $M = 8:2$ (4 : 1), a sharp single peak was revealed at 39 °C, which was close to the physiological temperature of the human body (37 °C). Accordingly, we chose the binary mixtures of the two fatty acids (PCM) with a mass ratio of 8 : 2 as the switch of temperature responsiveness.

Further characterization of the PCM was performed by the Fourier transform infrared (FT-IR) spectroscopy and X-ray diffraction (XRD) techniques. The FT-IR spectra were measured to evaluate the synthesis of the PCM. As shown in Fig. S1b (ESI†), LA, SA and PCM had the same peaks; 2924 cm^{-1} and 2855 cm^{-1} were the symmetrical and asymmetrical stretching vibration absorption of $-CH_2$, 1710 cm^{-1} was the stretching vibration absorption of C═O and 943 cm^{-1} was the out-of-plane deformation vibration of O–H. LA and SA are fatty acids with different numbers of carbon atoms so they had the same main characteristic peaks. Compared with LA and SA, the FT-IR spectrum of the PCM (the mixture of LA and SA) was not a simple stacking of both. It turns out that physical interactions existed after melt blending of the two fatty acids such as weak van der Waals forces between hydrocarbon chains and strong hydrogen bonds between polar groups.[23] The X-ray diffraction (XRD) pattern (Fig. S1c, ESI†) confirms the crystal structure of the eutectic mixture and indicates that the heating process has no influence on the structure.[24]

3.2. Characterization of the electrospun fibers

The morphological structure, size and distribution pattern of the diameter influence the drug release and mechanical properties of the fibers.[25] Hence, we utilized SEM and TEM to observe the morphology of the nanofibers. Fig. S2 (ESI†) and Fig. 1a–c exhibit the morphology of pure PCL, PU fibers and PU–PCL core–shell fibers with different content of PCM. All the fibers showed random arrangements without beads. In the process of coaxial electrospinning, the shell solution forms a shell containing the inner solution, which can inhibit the Rayleigh instability of the solution and also reduce the surface tension at the boundary between the two solutions. The combination of the two solutions makes the fibers more uniform. Therefore, the core–shell nanofibers show more uniform morphology than pure PCL and PU nanofibers.[26,27] Furthermore, the diameters of the nanofibers were significantly influenced by the fiber structure. As Fig. S3f (ESI†) indicates, coaxial nanofibers possessed larger average diameters than uniaxial nanofibers.[28,29] Additionally, the coaxial nanofibers PU–PCL/PCM1 and PU–PCL/PCM2 incorporated with PCM in the shell showed narrower distributions than the pure PU–PCL coaxial nanofibers, which can likely be attributed to the decrease in viscosity after incorporation of the PCM.[30–33] The diameter distribution histograms of the series of nanofibers also revealed the trend (Fig. S3, ESI†). The core and sheath of the coaxial nanofiber were observed obviously from the TEM image of a PU–PCL/PCM2 fiber (Fig. 1d). Significantly, PU was completely wrapped by PCL.

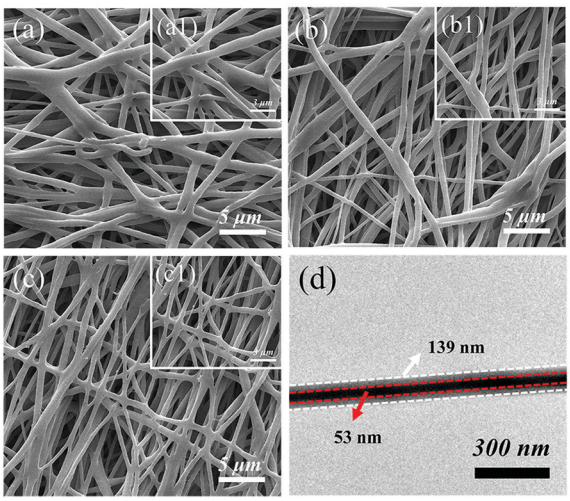

Fig. 1 Characterization of the morphology of the fibers. SEM graphs of (a) PU–PCL core–shell fibers, (b) PU–PCL/PCM1 core–shell fibers (f_{PCM} = 0.05) and (c) PU–PCL/PCM2 core–shell fibers (f_{PCM} = 0.1). (d) TEM images of PU–PCL/PCM1 core–shell fibers.

FT-IR spectra were measured to investigate the preparation of temperature-responsive core–shell fibers. As shown in Fig. S4a (ESI†), the characteristic peaks of PCL were observed at 2946 cm^{-1} (asymmetric CH_2 stretching), 2865 cm^{-1} (symmetric CH_2 stretching), 1724 cm^{-1} (C═O stretching) and 1242 cm^{-1} (asymmetric C–O–C stretching).[34] The PU-related peaks appeared approximately at 3432 cm^{-1} (–NH stretching) and 1538 cm^{-1} (–NHCO stretching). The FT-IR spectrum of HCPT–PU–PCL/PCM presented peaks at 3436 cm^{-1}, 1728 cm^{-1} (C═O stretching), 1242 cm^{-1} (asymmetric C–O–C stretching) and 936 cm^{-1} (out-of-plane deformation vibration of –OH). Thus, the characteristic peaks in the composite fiber clearly verified the successful preparation of PCM loaded core–shell fibers.[35] Fig. S4c (ESI†) shows the DSC thermograms for the fiber samples of PU–PCL/PCM1 (f_{PCM} = 0.05) and PU–PCL/PCM2 (f_{PCM} = 0.1). Two peaks were presented at approximately 39 and 56 °C, which were attributed to the PCM and PCL, respectively. The result further proved that the PCM was successfully composited into the core–shell fibers. Moreover, the results indicated that the PCM was phase-separated in the fibers and no strong interactions influenced the melting of the PCM. The intensities of the PCM peaks clearly decreased with decreasing mass of PCM in the fibers. Additionally, a slight decrease of melting temperature for the fibers with increasing PCM was observed. As shown in Fig. S4b (ESI†), the absence of diffraction peaks in the XRD pattern indicated that PU was amorphous with no clear indication of crystallinity. PCL had two diffraction peaks due to its semi-crystalline nature. However, the composite fibers (PU–PCL, PU–PCL/PCM1, and PU–PCL/PCM2) only showed two peaks at 21.4 and 23.7° owing to the crystalline diffraction for the PCL chain segment.[25,36] No characteristic peaks of the PCM were observed in the coaxial fibers. It can be hypothesized that all the PCM in the coaxial fibers is amorphous and is evenly distributed.[37,38]

Favorable mechanical integrity is indispensable to a successful drug delivery platform that should be able to withstand the stress *in vivo* and temporal loading regimes after being implanted.[25] Poor mechanical properties can bring a potential

threat of treatment failure and are not conductive to integration with surrounding tissue. To confirm that the prepared fiber mats have enough mechanical strength to maintain integrity and stability *in vivo*, the mechanical properties of the mats were evaluated.[39,40] Obviously, the maximum elongation of the PU–PCL/PCM1 coaxial fibers was significantly higher than that of pure PCL fibers while keeping a higher modulus and tensile strength (Fig. 2a and b). As shown in Fig. 2c and Fig. S5 (ESI†), the stress–strain curves, mechanical property histogram and data of the fiber mats are presented. The pure PCL fibers exhibited a tensile strength of only 5.3 MPa and the coaxial PU–PCL fibers exhibited a tensile strength of 20.5 ± 0.4 MPa, approximately fourfold that of the pure PCL fibers. Fiber mats PU–PCL/PCM1 and PU–PCL/PCM2 also exhibited improved tensile strength that reached 19 and 17.1 MPa, respectively (Fig. S5a, ESI†). In addition, the Young's moduli of the fibers showed a similar trend (Fig. S5c, ESI†). The Young's moduli were 69.3 ± 0.6, 43.3 ± 1.6, 41.22 ± 0.8, and 24.8 ± 1.1 MPa for the PU–PCL, PU–PCL/PCM1, PU–PCL/PCM2, and PCL mats, respectively (Table S1, ESI†). Similarly, the PU–PCL coaxial fiber mats indicated a significant improvement of the elongation at break (Fig. S5b, ESI†). The elongation at break of the fiber mats presented a linear increase gradually from 77.2% for PCL to 169.5, 178.3 and 221.4 for the PU–PCL, PU–PCL/PCM1, and PU–PCL/PCM2 mats, respectively. All the results exhibited that PU as a reinforcement and toughening material incorporated in composite nanofibers clearly enhanced the mechanical properties including the tensile strength and elongation at break compared with pure PCL fibers. Additionally, it turned out that the incorporation of the PCM into the coaxial fibers decreased the tensile strength and Young's moduli to some extent. Generally, there is a positive correlation between the material tensile strength and intermolecular force and greater intermolecular force will usually provide polymers with stronger tensile properties.[41–43] Hence, we speculate that the PCM with low molecular weight reduced the interaction between polymer chains leading to lower tensile strength of the PU–PCL/PCM1 and PU–PCL/PCM2 mats. Moreover, integration of a PCM into polymers could reduce inflexibility and improve the flexibility, as indicated by the Young's moduli and elongation at break of the composite. The mechanical properties, as indicated by the prepared fibers with the appropriate mechanical properties, confirmed that the coaxial fiber membranes are durable enough for clinical application and are promising materials as implantable drug delivery devices.

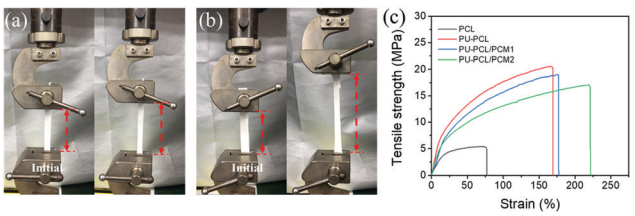

Fig. 2 Mechanical properties of the fibers. Photograph of (a) the PCL fibrous membrane *versus* (b) the PU–PCL/PCM1 fibrous membrane under a tensile test, and (c) stress–strain curves of different fibrous membranes.

3.3. *In vitro* drug release studies

To investigate the drug release profiles, the fiber mats were immersed in PBS (pH 7.4, to mimic the physiological environment) under different conditions. The fluorescence optical micrograph of the core–shell fibers obviously indicated that rhodamine B was encapsulated in the fibers (Fig. S6, ESI†).[43] The core–shell fibers exhibited a characteristic absorption peak at 553 nm in UV-vis spectroscopy, further verifying the successful encapsulation of the model drug (rhodamine B) in the composite fiber (Fig. S7, ESI†).[44] Additionally, UV-vis spectroscopy indicated no change at different temperatures, revealing the stability of the drug delivery system.[45]

Fig. 3a indicates the release performance of model drug rhodamine B in coaxial nanofiber mat PU–PCL/PCM2 (f_{PCM} = 0.1) at various temperatures. It can be visually observed that fiber mat PU–PCL/PCM2 showed similar release profiles at 25 and 37 °C, which was a result of the controlled release by the coaxial structure of the fibers. In other words, the drug release rate slowed down below 39 °C. The membranes released 34.4% and 37.2% of the drugs at 25 °C and 37 °C over 10 h, respectively. This phenomenon can be assigned to the enrichment of partial rhodamine B on the fiber surface during electrospinning. Even though the rhodamine B was supposed to be completely encapsulated in the core of the nanofibers, the model drug molecules tended to migrate to the surface of the polymer due to the electrostatic interactions in the high voltage electrospinning process so that they cannot be completely encapsulated in the PU core fiber. Furthermore, the great solubility in water and small molecular weight cause rhodamine B to permeate into the water medium from the polymer. Hence, the

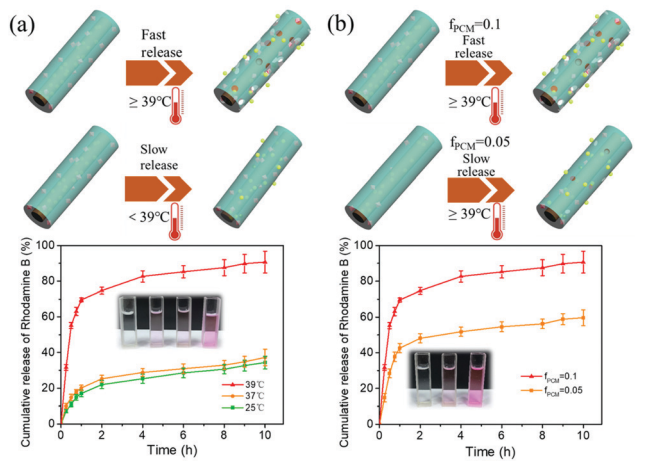

Fig. 3 (a) Release profiles at 25, 37 and 39 °C of model drug rhodamine B from PU–PCL/PCM2 fibers (f_{PCM} = 0.1) in PBS at pH 7.4; the inset is the release media under different temperatures at 2 h (from left to right are pure PBS solution, and release media at 25, 37 and 39 °C, respectively); the upside is the illustration of the drug release mechanism under different temperatures. (b) Release profiles at 39 °C of rhodamine B from PU–PCL/PCM1 fibers (f_{PCM} = 0.05) and PU–PCL/PCM2 fibers (f_{PCM} = 0.1) in a PBS buffer solution at pH 7.4; the inset is the release media for PU–PCL/PCM1 and PU–PCL/PCM2 at 2 h, 39 °C (from left to right are pure PBS solution, and release media for PU–PCL/PCM1 and PU–PCL/PCM2, respectively); the upside is the illustration of the drug release mechanism for the fibers with different content of PCM.

release profile presents a certain release of rhodamine B below 39 °C. In contrast, on heating at 39 °C, the fiber mats PU–PCL/PCM2 allowed a significantly fast release (approximately 90% of rhodamine B released) over the same period. The color of the release media under different temperatures at 2 h also obviously showed the different release rate of the fibers and the shade of the color depends on the amount of release of rhodamine B; a darker color indicates more release. The fast release could be attributed to the melting of the PCM incorporated in the PCL sheath under the phase transition temperature. Pores formed with the melting of the PCM, leading to increasing paths for molecules to move from the fibers. Drug release from polymer carriers can be classified into two types: (i) release with the degradation or erosion of polymer matrixes and (ii) release *via* diffusion from polymer matrixes.[46] The pores in the fibers accelerated the erosion rates of the polymer matrixes and produced more paths that can promote molecules to diffuse from the polymer matrixes. Furthermore, Fig. 3b indicates the release curves of the fiber mats PU–PCL/PCM1 and PU–PCL/PCM2 at 39 °C. The fiber mats with different content of PCM in the PCL sheath presented diverse release rates under the same conditions. During 2 h, ~74% of rhodamine B was released from the sample PU–PCL/PCM2 and the remaining rhodamine B was released gently and sustainably during 8 h. Nevertheless, the release of rhodamine B from fiber mat PU–PCL/PCM1 to the media was slow and only ~48% of the model drug was released during 2 h. Similarly, the remaining rhodamine B was released slowly and sustainably and the PU–PCL/PCM1 mat only allowed the release of ~59% during 10 h. In a word, the cumulative rhodamine B release for the PU–PCL/PCM2 mat was higher than that of the PU–PCL/PCM1 mat. This can be attributed to the differences of the amount of PCM in the PCL sheath of the fibers, which led to differences in pore size, aperture distribution and surface area when the PCM melted at 39 °C. The color of the release media for the two membranes also obviously showed the same trend.

In this paper, a zero-order kinetic model, first-order kinetic model, Higuchi kinetic model, Korsmeyer–Peppas empirical model and biexponential and biphasic kinetic model were used to fit the *in vitro* release data. *R*-Squared (R^2) is used to judge the degree of fitting.[47–53] As Table 1 indicates, the biexponential and biphasic kinetic model ($R^2 > 0.99$) shown in eqn (4) could be applied to analyze the release mechanism of rhodamine B from the coaxial fibers PU–PCL/PCM1 and PU–PCL/PCM2 at 39 °C.

$$Q_0 - Q = Ae^{\alpha t} + Be^{\beta t} \quad (4)$$

The biexponential and biphasic kinetic model consists of fast (burst release) and slow (sustained release) phases. The fast phase reflects the burst release effect of the drug carrier on the initial release and the slow phase reflects the controlled release effect of the drug carrier. In this equation, Q_0 is a constant; Q represents the cumulative drug release rate; and α and β are the release rate constants of burst release and sustained release, respectively. A and B are the kinetic constants of burst release and sustained release, respectively.

Table S2 (ESI†) plots the experimental data after fitting eqn (1). The fitting results were perfectly consistent with the release behavior; in the initial periods, the PCM melted at 39 °C, which contributed to the burst release of the rhodamine B in the surface of the fibers to the PBS buffer, whereas in the middle and later periods, the remaining model drug slowly diffused from the core of the fibers and was released sustainably to the medium (Fig. S8, ESI†).

3.4. Cell viability

The cytotoxicity assessment shown in Fig. S9 (ESI†) confirmed the nontoxicity of the prepared coaxial fibers. Obviously, the extracts of the fibers indicated a significant effect on the cell viability.[54,55] HCPT was chosen as a model anticancer drug. To verify the structure of HCPT loaded in the membrane, the FT-IR spectra were investigated. As indicated in Fig. S10 (ESI†), the stretching vibration absorption of C═O (1728 cm^{-1}) moved to a lower wave number (1700 cm^{-1}) when HCPT was loaded in the membrane. This indicated that hydrogen bonds exist between the drug molecule and the carrier. We speculate that the hydrogen bonds formed between –OH of HCPT and –C═O of the polymer. To further evaluate the temperature-responsive drug release of the core–shell fibers, the cell viability after treatment with the extract was examined using the HepG2 cell line as model cancer cells.[56] The *in vitro* release of HCPT from the coaxial fibers was performed in DMEM at 25, 37 and 39 °C.[57] The extracts were collected 24 h and 48 h after incubation. The groups of PU–PCL and PU–PCL/PCM were investigated for a control. MTT assay was applied to evaluate

Table 1 Results of fitting the curves of *in vitro* release

	Model	Regression equation	R^2
PU–PCL/PCM1	Zero order kinetics	$Q = 0.26t + 0.0402$	0.6227
	First order kinetics	$\ln(1 - Q) = -0.0654t - 0.3594$	0.7296
	Higuchi	$Q = 0.1288t^{1/2} + 0.2217$	0.8079
	Korsmeyer–Peppas	$\ln Q = 3.5868 + 0.2316 \ln t$	0.8751
	Biexponential and biphasic kinetics	$0.2334 - Q = 0.5785e^{-2.3159t} + 0.7002e^{-0.0171t}$	0.9987
PU–PCL/PCM2	Zero order kinetics	$Q = 0.4563t + 0.0549$	0.5505
	First order kinetics	$\ln(1 - Q) = -0.2585t - 0.6331$	0.7962
	Higuchi	$Q = 0.2219t^{1/2} + 0.3021$	0.7529
	Korsmeyer–Peppas	$\ln Q = 4.1176 + 0.1835 \ln t$	0.8736
	Biexponential and biphasic kinetics	$0.9337 - Q = 0.2813e^{-0.2188t} + 0.9086e^{-3.8156t}$	0.9984

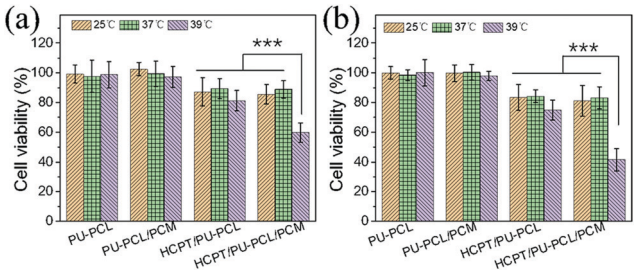

Fig. 4 HepG2 cell viability quantified by MTT assay. The cells were treated with the release media for (a) 24 h and (b) 48 h.

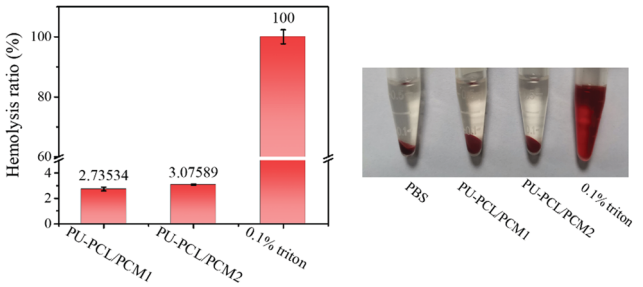

Fig. 5 (a) Hemolytic percentage and (b) pictures from the hemolytic activity test of the PU–PCL/PCM core–shell fibers.

the cell viability after treatment with the extract for 24 h and 48 h (Fig. 4a and b). It is obvious that temperature had a negligible influence on cell viability when treating the cell with extracts of the HCPT–PU–PCL mat. On the other hand, the cell viability was clearly lower when treating with HCPT-release media of HCPT–PU–PCL/PCM mats at 39 °C compared with lower temperatures (25 and 37 °C). Furthermore, the HCPT–PU–PCL/PCM mat presented prominent lower cell viability than the HCPT–PU–PCL mat at 39 °C. This result showed that the PCM played a role in temperature responsiveness. Both incubation times (24 h and 48 h) exhibited a similar trend. Therefore, the cytotoxicity test further proved the temperature-responsiveness of the drug delivery system.

Good biocompatibility is essential to drug carriers. An *in vitro* hemolysis test was performed to evaluate the hemocompatibility of the PU–PCL/PCM membranes. Fig. 5b indicates the significant difference in color between the two electrospun membranes, PBS (negative control) and 0.1% Triton X-100 (positive control). The electrospun membrane groups were almost transparent, which was similar to the negative control group, while the positive group was bright red. As shown in Fig. 5a, the PU–PCL/PCM1 and PU–PCL/PCM2 membranes exhibited very low hemolysis ratios (2.7% and 3.1%, respectively). When the amount of PCM was added, the hemolysis ratios showed no obvious increase.

4. Conclusion

In this work, we have successfully presented a tunable temperature-responsive site-specific drug-delivery platform, comprising PU–PCL composite elctrospun fibers incorporated with PCM by a simple coaxial electrospinning technique. The PCM-functionalized coaxial fibers exhibited a uniform core–sheath morphology that could enhance the controlled release with a core of PU and a PCL shell and showed enhanced mechanical properties to meet requirements for cancer treatment after implantation. The *in vitro* release profiles and the result of cytotoxicity indicated that the encapsulated molecules were released significantly faster above 39 °C than those at lower temperatures within the same incubation time. More importantly, the release profiles were analyzed by different kinetic models and the result indicated that the release of the drug from the nanofibers followed fast and slow biphasic release kinetics, which is promising in multidrug packaging for synergistic therapies. In fact, the system has potential to be combined with photothermal therapy (PTT) and we anticipate that the drug delivery system could perform as an effective platform for tumor therapy.

Ethical statement

There is no ethical conflict in this work. This work includes cell viability tests and hemolysis tests. Only cells (HepG2/L929) (commercial) and sheep blood (commercial) were used. No live animal subject is involved in this work.

Conflicts of interest

The authors declare that they have no conflict of interest.

Acknowledgements

National Natural Science Foundation of China (No. 21774060), National Key R&D Program of China (2017YFF0207804), Jiangsu Key Lab of Biomass-based Energy and Materials (JSBEM2016011), State Key Laboratory for Mechanical Behavior of Materials (20171914), Priority Academic Program Development of Jiangsu Higher Education Institutions (PAPD), Top-notch Academic Programs Project of Jiangsu Higher Education Institutions (TAPP) and Natural Science Key Project of the Jiangsu Higher Education Institutions (16KJA220006) are acknowledged with gratitude. We also thank Advanced Analysis & Testing Center, Nanjing Forestry University, for SEM characterization.

References

1 S. Gao, G. Tang, D. Hua, R. Xiong, J. Han, S. Jiang, Q. Zhang and C. Huang, *J. Mater. Chem. B*, 2019, **7**, 709–729.
2 J. Xue, C. Zhu, J. Li, H. Li and Y. Xia, *Adv. Funct. Mater.*, 2018, **28**, 1705563.
3 M. Zhang, C. C. Song, S. Su, F. S. Du and Z. C. Li, *ACS Appl. Mater. Interfaces*, 2018, **10**, 7798–7810.
4 C. Huang, S. J. Soenen, J. Rejman, J. Trekker, L. Chengxun, L. Lagae, W. Ceelen, C. Wilhelm, J. Demeester and S. C. De Smedt, *Adv. Funct. Mater.*, 2012, **22**, 2479–2486.
5 L. Weng and J. W. Xie, *Curr. Pharm. Des.*, 2015, **21**, 1944–1959.
6 X. Miao, J. Lin and F. Bian, *J. Bioresour. Bioprod.*, 2020, **5**, 26–36.

7 J. Y. Zhang, X. Wang, T. J. Liu, S. Liu and X. B. Jing, *Drug Delivery*, 2016, **23**, 794–800.
8 Z. Xia, J. Li, J. Zhang, X. Zhang, X. Zheng and J. Zhang, *J. Bioresour. Bioprod.*, 2020, **5**, 79–95.
9 J. Zeng, L. X. Yang, Q. Z. Liang, X. F. Zhang, H. L. Guan, X. L. Xu, X. S. Chen and X. B. Jing, *J. Controlled Release*, 2005, **105**, 43–51.
10 J. N. Li, Q. Y. Gong, W. G. Xu, K. Zhang and T. J. Liu, *J. Controlled Release*, 2017, **259**, E59–E59.
11 P. Wen, K. Feng, H. Yang, X. Huang, M. H. Zong, W. Y. Lou, N. Li and H. Wu, *Carbohydr. Polym.*, 2017, **169**, 157–166.
12 H. S. Yoo, T. G. Kim and T. G. Park, *Adv. Drug Delivery Rev.*, 2009, **61**, 1033–1042.
13 Z. F. Guo, G. S. Tang, Y. H. Zhou, S. W. Liu, H. Q. Hou, Z. Y. Chen, J. H. Chen, C. H. Hu, F. Wang, S. C. De Smedt, R. H. Xiong and C. B. Huang, *Carbohydr. Polym.*, 2017, **169**, 198–205.
14 J. L. Li, Y. J. Cheng, C. Zhang, H. Cheng, J. Feng, R. X. Zhuo, X. Zeng and X. Z. Zhang, *ACS Appl. Mater. Interfaces*, 2018, **10**, 5287–5295.
15 D. W. Wei, H. Wei, A. C. Gauthier, J. Song, Y. Jin and H. Xiao, *J. Bioresour. Bioprod.*, 2020, **5**, 1–15.
16 H. Kweon, M. K. Yoo, I. K. Park, T. H. Kim, H. C. Lee, H. S. Lee, J. S. Oh, T. Akaike and C. S. Cho, *Biomaterials*, 2003, **24**, 801–808.
17 D. W. Hua, Z. C. Liu, F. Wang, B. H. Gao, F. Chen, Q. L. Zhang, R. H. Xiong, J. Q. Han, S. K. Samal, S. C. De Smedt and C. B. Huang, *Carbohydr. Polym.*, 2016, **151**, 1240–1244.
18 Q. H. Feng, W. X. Zhang, Y. Z. Li, X. M. Yang, Y. W. Hao, H. L. Zhang, W. Li, L. Hou and Z. Z. Zhang, *Nanoscale*, 2017, **9**, 15685–15695.
19 G. D. Moon, S. W. Choi, X. Cai, W. Y. Li, E. C. Cho, U. Jeong, L. V. Wang and Y. N. Xia, *J. Am. Chem. Soc.*, 2011, **133**, 4762–4765.
20 Q. Li, L. H. Sun, M. M. Hou, Q. B. Chen, R. H. Yang, L. Zhang, Z. G. Xu, Y. J. Kang and P. Xue, *ACS Appl. Mater. Interfaces*, 2019, **11**, 417–429.
21 Z. Jin, K. Q. Wu, J. W. Hou, K. H. Yu, Y. Y. Shen and S. R. Guo, *Biomaterials*, 2018, **153**, 49–58.
22 N. Zhang, M. H. Li, X. T. Sun, H. Z. Jia and W. G. Liu, *Biomaterials*, 2018, **159**, 25–36.
23 Q. S. Chen, C. L. Zhu, D. Huo, J. J. Xue, H. Y. Cheng, B. H. Guan and Y. N. Xia, *Nanoscale*, 2018, **10**, 22312–22318.
24 J. J. Xue, M. He, H. Liu, Y. Z. Niu, A. Crawford, P. D. Coates, D. F. Chen, R. Shi and L. Q. Zhang, *Biomaterials*, 2014, **35**, 9395–9405.
25 A. P. Tiwari, T. I. Hwang, J. M. Oh, B. Maharjan, S. Chun, B. S. Kim, M. K. Joshi, C. H. Park and C. S. Kim, *ACS Appl. Mater. Interfaces*, 2018, **10**, 20256–20270.
26 Y. Dzenis, *Science*, 2004, **304**, 1917–1919.
27 D. G. Yu, J. H. Yu, L. Chen, G. R. Williams and X. Wang, *Carbohydr. Polym.*, 2012, **90**, 1016–1023.
28 M. M. Zhu, R. H. Xiong and C. B. Huang, *Carbohydr. Polym.*, 2019, **205**, 55–62.
29 S. X. Chen, S. K. Boda, S. K. Batra, X. R. Li and J. W. Xie, *Adv. Healthcare Mater.*, 2018, **7**, 20.
30 B. Schoen, R. Avrahami, L. Baruch, Y. Efraim, I. Goldfracht, O. Elul, T. Davidov, L. Gepstein, E. Zussman and M. Machluf, *Adv. Funct. Mater.*, 2017, **27**, 9.
31 C. Q. You, Z. G. Gao, H. S. Wu, K. Sun, L. K. Ning, F. Lin, B. W. Sun and F. Wang, *J. Mater. Chem. B*, 2019, **7**, 314–323.
32 M. X. Hu, F. Teng, H. Y. Chen, M. M. Jiang, Y. Z. Gu, H. L. Lu, L. F. Hu and X. S. Fang, *Adv. Funct. Mater.*, 2017, **27**, 9.
33 Y. K. Sung, B. W. Ahn and T. J. Kang, *J. Magn. Magn. Mater.*, 2012, **324**, 916–922.
34 J. J. Xue, Y. Z. Niu, M. Gong, R. Shi, D. F. Chen, L. Q. Zhang and Y. Lvov, *ACS Nano*, 2015, **9**, 1600–1612.
35 S. Y. Cheng, Y. Jin, N. X. Wang, F. Cao, W. Zhang, W. Bai, W. F. Zheng and X. Y. Jiang, *Adv. Mater.*, 2017, **29**, 8.
36 A. H. Najafabadi, A. Tamayol, N. Annabi, M. Ochoa, P. Mostafalu, M. Akbari, M. Nikkhah, R. Rahimi, M. R. Dokmeci, S. Sonkusale, B. Ziaie and A. Khademhosseini, *Adv. Mater.*, 2014, **26**, 5823–5830.
37 Y. W. Deng, J. Ling and M. H. Li, *Nanoscale*, 2018, **10**, 6781–6800.
38 G. D. Liu, Z. B. Gu, Y. Hong, L. Cheng and C. M. Li, *J. Controlled Release*, 2017, **252**, 95–107.
39 S. Choi, Y. Choi, M. S. Jang, J. H. Lee, J. H. Jeong and J. Kim, *Adv. Funct. Mater.*, 2017, **27**, 9.
40 Y. Y. Yue, X. H. Wang, J. Q. Han, L. Yu, J. Q. Chen, Q. L. Wu and J. C. Jiang, *Carbohydr. Polym.*, 2019, **206**, 289–301.
41 C. C. Chen, H. Y. Wang, S. Y. Li, L. Fang and D. G. Li, *Cellulose*, 2017, **24**, 5487–5493.
42 Y. Q. Qiao, C. P. Shi, X. L. Wang, P. P. Wang, Y. C. Zhang, D. Y. Wang, R. R. Qiao, X. C. Wang and J. Zhong, *ACS Appl. Mater. Interfaces*, 2019, **11**, 5401–5413.
43 S. Ye, Z. J. Zhu, Y. Y. Wen, C. Su, L. Jiang, S. He and W. Shao, *Polymers*, 2019, **11**, 11.
44 U. Bozuyuk, O. Yasa, I. C. Yasa, H. Ceylan, S. Kizilel and M. Sitti, *ACS Nano*, 2018, **12**, 9617–9625.
45 M. B. Qi, X. H. Li, Y. Yang and S. B. Zhou, *Eur. J. Pharm. Biopharm.*, 2008, **70**, 445–452.
46 S. Y. Nie, W. J. Lin, N. Yao, X. D. Guo and L. J. Zhang, *ACS Appl. Mater. Interfaces*, 2014, **6**, 17668–17678.
47 L. L. Lao and S. S. Venkatraman, *J. Controlled Release*, 2008, **130**, 9–14.
48 S. K. Poovathingal, N. Kravchenko-Balasha, Y. S. Shin, R. D. Levine and J. R. Heath, *Small*, 2016, **12**, 1425–1431.
49 M. Y. Hei, J. Wang, K. Wang, W. P. Zhu and P. X. Ma, *J. Mater. Chem. B*, 2017, **5**, 9497–9501.
50 Q. Y. Bao, B. Newman, Y. Wang, S. Choi and D. J. Burgess, *J. Controlled Release*, 2018, **276**, 93–101.
51 S. L. Madurai, S. W. Joseph, A. B. Mandal, J. Tsibouklis and B. S. R. Reddy, *Nanoscale Res. Lett.*, 2011, **6**, 8.
52 M. Cerea, A. Maroni, L. Palugan, M. Bellini, A. Foppoli, A. Melocchi, L. Zema and A. Gazzaniga, *J. Controlled Release*, 2018, **287**, 247–256.
53 K. Kosmidis and P. Macheras, *Int. J. Pharm.*, 2018, **543**, 269–273.
54 G. S. Tang, R. H. Xiong, D. Lv, R. X. Xu, K. Braeckmans, C. B. Huang and S. C. De Smedt, *Adv. Sci.*, 2019, **6**, 9.
55 G. C. J. Barretina, N. Stransky, K. Venkatesan, A. A. Margolin, S. Kim, C. J. Wilson, J. Lehár, G. V. Kryukov and D. Sonkin, *Nature*, 2012, **483**, 603–607.
56 W. M. D. K. C. Nicolaou, *Angew. Chem., Int. Ed.*, 2010, **30**, 1387–1416.
57 J. Jiang, J. Xie, B. Ma, D. E. Bartlett, A. Xu and C. H. Wang, *Acta Biomater.*, 2014, **10**, 1324–1332.